applied sciences

MDPI

Article

Effect of High-Mass Fraction of Aluminum on Catalytic Hybrid Rocket Motor

Hui Tian [1,2], Zhongshuo Wang [1,2], Hao Zhu [1,2,*], Yudong Lu [1,2], Jingfei Gao [1,2] and Guobiao Cai [1,2]

[1] School of Astronautics, Beihang University, Beijing 100191, China
[2] Key Laboratory of Spacecraft Design Optimization & Dynamic Simulation Technologies, Ministry of Education, Beijing 102206, China
* Correspondence: zhuhao@buaa.edu.cn

Abstract: Catalytic hybrid rocket motors using hydrogen peroxide (HP) are easy and efficient to achieve multiple starts and stops, and hydroxyl-terminated polybutadiene (HTPB) grains are commonly used due to their excellent mechanical properties. The low regression rate of HTPB grains limits the application of hybrid rocket motors. Furthermore, the addition of solid aluminum particles can effectively improve the regression rate and performance of hybrid rocket motors. However, the experimental results of a high mass fraction of aluminum and hydrogen peroxide available at present are not sufficient. In this research, the impact of a high mass fraction of aluminum on the motor performance and ablation rate of nozzles is studied experimentally. A solution of 95% hydrogen peroxide and HTPB with an aluminum additive are adopted as propellants. The variation in the axial regression rate of the grains is obtained by computed tomography (CT) scans and pre-test parameter measurements. The instantaneous regression rate method is adopted to obtain the real-time regression rate of the motor. The surface appearance and composition of the front and the end of the grains after the tests are analyzed by electron microscopy. Carbon ceramic and tungsten-bronze nozzles are used to explore the effect of a high mass fraction of aluminum on nozzle ablation. The experimental results show that the addition of aluminum raises the specific impulse and decreases the optimal oxygen-to-fuel ratio of the propellant combination. The high mass fraction of the aluminum particles has a severe ablative effect on carbon ceramic nozzles, while the effect on tungsten-bronze nozzles is minimal for a hot test lasting four to five seconds. Our results can provide experimental guidance for the application of a high mass fraction of aluminum and hydrogen peroxide hybrid rocket motor.

Keywords: experimental study; high-performance hybrid rocket motors; performance evaluation; nozzle ablation

check for updates

Citation: Tian, H.; Wang, Z.; Zhu, H.; Lu, Y.; Gao, J.; Cai, G. Effect of High-Mass Fraction of Aluminum on Catalytic Hybrid Rocket Motor. *Appl. Sci.* **2022**, *12*, 13023. https://doi.org/10.3390/app122413023

Academic Editor: Saulius Juodkazis

Received: 8 November 2022
Accepted: 13 December 2022
Published: 19 December 2022

Publisher's Note: MDPI stays neutral with regard to jurisdictional claims in published maps and institutional affiliations.

Copyright: © 2022 by the authors. Licensee MDPI, Basel, Switzerland. This article is an open access article distributed under the terms and conditions of the Creative Commons Attribution (CC BY) license (https://creativecommons.org/licenses/by/4.0/).

1. Introduction

A hybrid rocket motor is a form of propulsion system that typically uses solid fuel and a liquid oxidizer [1,2]. Due to the benefits of hybrid rocket motors, such as multiple starts and stops, adaptable thrust adjustments, and superior safety, research on hybrid rocket motors has become a hot topic in recent years [3–5]. The regression rate is a crucial parameter in the operation of a hybrid rocket motor. The regression process directly contributes to the fuel mass flow rate and the oxygen–fuel ratio of the motor, which determines the specific impulse and thrust of hybrid rocket motors. The combustion of the hybrid rocket motor, which differs from other engines, is diffusion controlled [6–8]. During the operation of hybrid rocket motors, the gaseous oxidant flows over the channel of the solid fuel, the fuel is heated to produce pyrolysis products, and the pyrolysis products diffuse to react with gaseous oxidants. The heat transfer from the combustion zone maintains the pyrolysis of the fuel and determines the pyrolysis rate of the fuel. Due to diffusion combustion, the application of hybrid rocket motors is generally limited by the low regression rate.

Many researchers have conducted numerous studies to improve the regression rate of hybrid rocket motors. Injection schemes [9–12], fuel types [13–16], and the addition of fuel additives have been demonstrated to be constructive methods for improving the regression rate of the hybrid rocket motor. The injection type variation mainly improves the efficiency of mixing, which in turn enhances the heat transfer between the reaction zone and the fuel wall and consequently the regression rate. The formation of a low-viscosity liquid layer on the grain surface is the intrinsic difference between classical and non-classical combustion mechanisms, and this liquid layer contributes to a higher regression rate during the combustion process [17]. The addition of solid particles to the grain mainly enhances the energy release and results in the improvement of the flame temperature and heat feedback from the combustion products [18,19]. Meanwhile, the addition of solid particles effectively improves the density-specific impulse of the propellant combinations and reduces the optimal oxygen-to-fuel ratio. Shark et al. [20] reported that adding $NaBH_4$ and AlH_3 generates up to a 47% and 85% growth in the regression rate, respectively, compared to neat dicyclopentadiene. The characteristic velocity efficiency is not efficient and varies from 80% to 90%. Risha et al. [21] demonstrated that adding metal nanoparticle fuel additives to HTPB-based fuels can significantly benefit the regression rate. Aluminum particles are a common metal addition to grains. The inclusion of aluminum particles within fuels can lead to an increase in the specific impulse, volumetric heat of oxidation, adiabatic flame temperature, heat of combustion, and radiative heat transfer [22]. Our previous findings [23] have shown that the addition of aluminum is more efficient than the addition of aluminum hydride for the enhancement of the regression rate. There exists a limit in how much aluminum can be added to a propellant. The inclusion of aluminum particles increases the regression rate of the propellant combination. However, the combustion becomes less efficient and the nozzle ablation can be aggravated when an excessive amount of aluminum particles are added.

The purpose of this study is to explore the influence of a high mass fraction of aluminum on the performance of motor and nozzle ablation. 95HP and HTPB with an aluminum additive are utilized as propellants. The experiment results indicate that adding aluminum particles into solid fuel boosts the average regression rate and reduces the optimal oxygen-to-fuel ratio. The addition of a high mass fraction of aluminum particles has a severe ablative effect on carbon ceramic nozzles, while the effect on tungsten-bronze nozzles is minimal for a hot test lasting four to five seconds.

2. Experimental Setup

Figure 1 displays a schematic of the test system. The motor mainly includes a hydrogen peroxide catalyst bed, a HTPB-based grain, a pre-combustion and a post-combustion chamber, and a Laval nozzle. The oxidizer feeding system is composed of a gas tank with high pressure, a hydrogen peroxide tank, a pressure regulator, hand valves, solenoid valves, pressure transducers, a mass flowmeter, a variable area cavitating venturi, and other components. A programmable logic controller (PLC) is employed to control the valves during the operation of the test. MultiscaleVoxel-1000 is used for the CT scans. A CMF025M/1700 flowmeter with a percentage error of 0.1% is adopted to measure the oxidizer mass flow rate. A CYB-601S thrust sensor is utilized to measure the engine thrust, and the measurement error is 0.1%. An electronic scale with an error of 0.1 g is utilized to weigh the mass of the motor before and after the experiment. A three-jaw caliper is adopted to measure the nozzle throat diameter before and after the experiment, and the measurement error is 0.01 mm. Table 1 shows the solid fuel formulas and nozzle material of the test motor. Table 2 lists the main design parameters of the test motor.

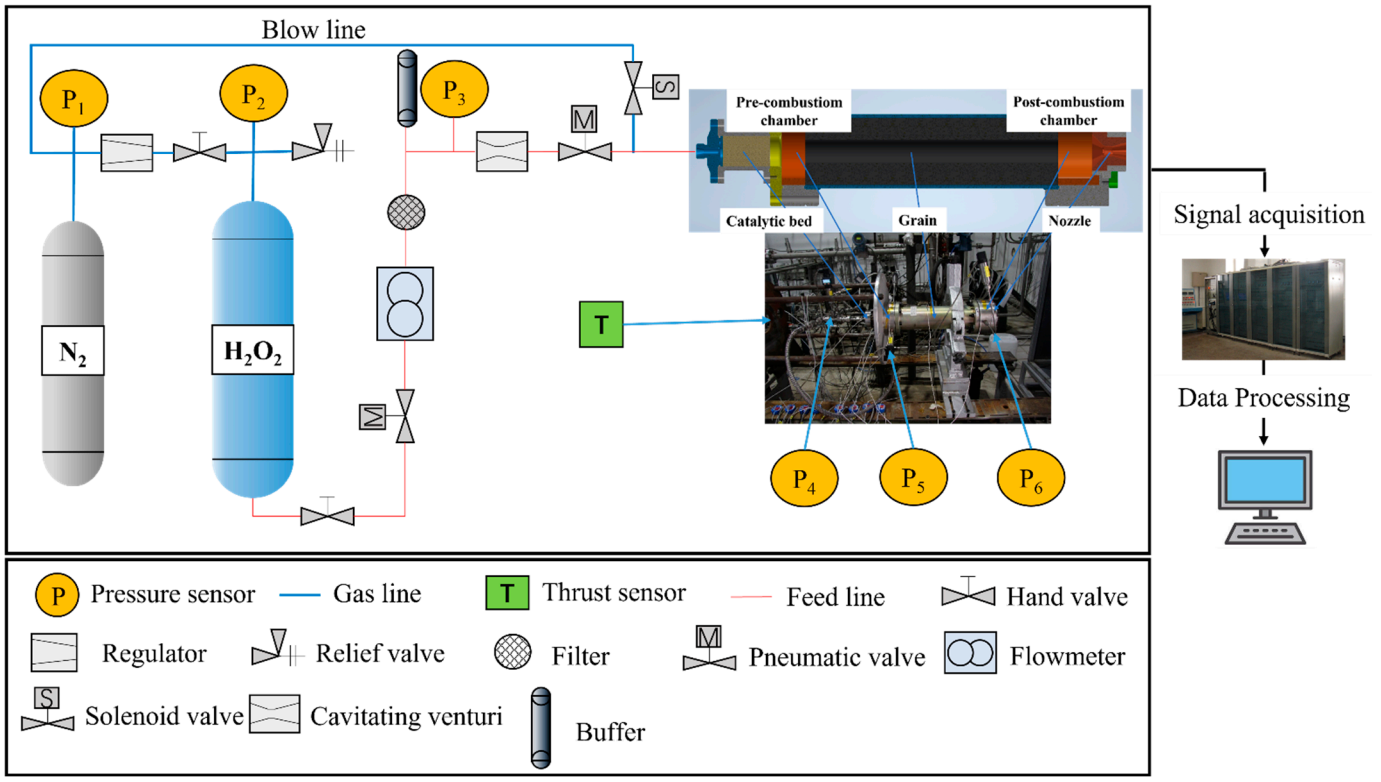

Figure 1. Schematic of the test system.

Table 1. Solid fuel formulas and nozzle material of the test motor.

Solid Fuel	Fuel Formula	ρ (g/cm^3)	Nozzle Material
A	35%HTPB + 65%Al	1.608	Tungsten–Copper Infiltration
B	42%HTPB + 58%Al	1.488	Carbon Ceramic
C	52%HTPB + 48%Al	1.343	Tungsten–Copper Infiltration
D	62%HTPB + 38%Al	1.214	Carbon Ceramic

where ρ is the density of the fuel.

Table 2. The main design parameters of the test motor.

Parameter	Unit	Value
Inner diameter of grain	mm	35
Outer diameter of grain	mm	100
Length of grain	mm	375
Inner diameter of pre-chamber	mm	80
Length of pre-chamber	mm	35
Inner diameter of post-chamber	mm	80
Length of post-chamber	mm	50
Diameter of nozzle throat	mm	15
Expansion ratio of nozzle	–	3

Based on a rocket propulsion analysis (RPA), the theoretical vacuum impulse and density impulse for the four grains of aluminum particles with mass fractions of 38%, 48%, 58%, and 65%, respectively, are calculated and analyzed. The combustion chamber pressure is 2 MPa and the expansion ratio of the nozzle is 3. Figure 2 shows the calculated results of the theoretical vacuum impulse and density impulse. The specific impulse of the propellant combination of HTPB-based grains with aluminum particles and 95% hydrogen peroxide is significantly higher than that of the propellant combination of HTPB-based grains without aluminum particles or 95% hydrogen peroxide with the region of the oxygen-to-fuel ratio

being from 1 to 4. The specific impulse increases slightly with the increase in the mass fraction of the aluminum particles at lower oxygen-to-fuel ratios, while it decreases with the increase in the mass fraction of the aluminum particles at higher oxygen-to-fuel ratios. Apparently, the addition of aluminum particles reduces the optimal oxygen-to-fuel ratio of the propellant combination, resulting in a miniaturized oxidizer tank. As can be seen in Figure 2b, the increase in the mass fraction of the aluminum particles in the grain has a significant effect on the increase in the density-specific impulse in the region of an oxygen-to-fuel ratio from 1 to 4.

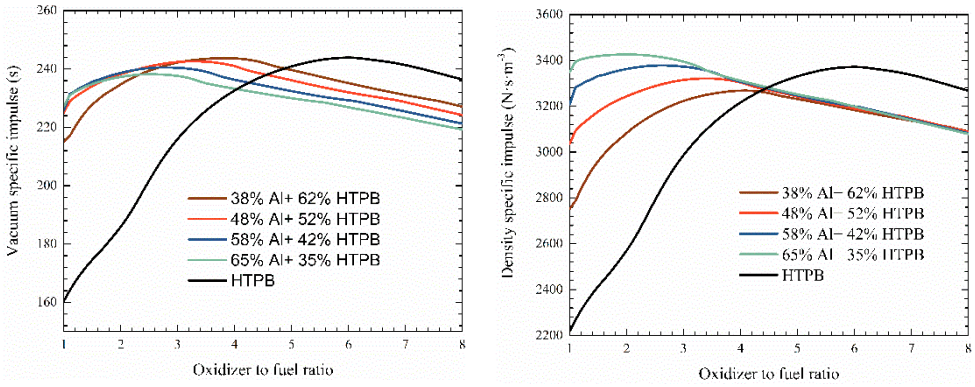

(**a**) (**b**)

Figure 2. Theoretical vacuum specific impulse and theoretical vacuum density-specific impulse. (**a**) Theoretical vacuum specific impulse. (**b**) Theoretical vacuum density-specific impulse.

3. Data Processing Method

The initial internal diameter of the grain is measured by vernier calipers before the test and the internal diameter of the grain after the test is measured by a CT scan. The calculation of Equations (1)–(6) refers to [23]. The average regression rate $\bar{\dot{r}}$ is obtained as:

$$\bar{\dot{r}} = \frac{r_e - r_i}{t} \tag{1}$$

where r_e is the initial inner radius of the grain, r_i is the final inner radius of the grain, and t is the working time of the motor.

Then the oxidizer mass flux G_o can be calculated as follows:

$$G_o = \frac{\dot{m}_o}{\pi r^2} \tag{2}$$

where $\dot{m}_o$ is the oxidizer mass flow rate, and r is the radius of the grain.

The combustion efficiency of the motor η_{c^*} is acquired by:

$$\eta_{c^*} = \frac{c^*}{{c_{th}}^*} \tag{3}$$

where ${c_{th}}^*$ is the theoretical characteristic velocity, which is calculated by RPA. c^* is obtained by:

$$c^* = \frac{\int_{t_0}^{t_w} p_c \cdot A_t dt}{\int_{t_0}^{t_w} (\dot{m}_f + \dot{m}_o) dt} \tag{4}$$

where p_c is the chamber pressure, A_t is the throat area of the nozzle, $\dot{m}_f$ is the mass flow rate of the fuel, t_w is the moment when the motor operation ends, and t_0 is the moment when the motor operation starts.

The specific impulse I_{sp} is acquired by:

$$I_{\mathrm{sp}} = \frac{\int_{t_0}^{t_w} F dt}{\int_{t_0}^{t_w} (\dot{m}_f + \dot{m}_o) dt} \tag{5}$$

where F is the thrust of the motor.

The ablation rate of nozzle r_s is obtained by:

$$r_s = \frac{d_2 - d_1}{2t} \tag{6}$$

where d_1 is the initial nozzle throat diameter, and d_2 is the final nozzle throat diameter.

For motors operating for long periods of time, the size of the grain passage varies significantly, and the oxidizer flux and regression rate change continuously during operation. In this paper, a method is developed to analyze the instantaneous regression rate of a hybrid rocket motor. By means of one or several tests, the change curve of the regression rate under different oxidizer flow rates can be obtained, and the regression rate equation can be fitted.

Assuming that the pressure of the combustion chamber measured in the test is $p_{c,\mathrm{exp}}$, and the combustion efficiency of the motor is η_{c*}, then by the equation for conservation of mass in the combustion chamber, the following equation can be given:

$$\dot{m}_f = \frac{p_{c,\mathrm{exp}} A_t}{c^* \eta_{c*}} - \dot{m}_o \tag{7}$$

During the operation of a hybrid rocket motor, the combustion chamber pressure and the oxygen–fuel ratio are continuously varied, and the theoretical characteristic velocity is a function of them. The value of c^* is obtained by a thermodynamic calculation:

$$c^* = f(p_c, r_{of}) \tag{8}$$

Moreover, the oxygen-to-fuel ratio r_{of} can be calculated as:

$$r_{of} = \frac{\dot{m}_o}{\dot{m}_f} = \frac{\dot{m}_o}{\frac{p_{c,\mathrm{exp}} A_t}{f(p_c, r_{of}) \eta_{c*}} - \dot{m}_o} \tag{9}$$

For a given test chamber pressure $p_{c,\mathrm{exp}}$, nozzle throat area A_t, combustion efficiency η_{c*}, and oxidizer flow rate $\dot{m}_o$, the oxygen-to-fuel ratio and fuel flow rate can be calculated iteratively from the above equation until the given accuracy is met:

$$\left| \dot{m}_o / \dot{m}_f - r_{of} \right| \leq \varepsilon \tag{10}$$

Based on the fuel mass flow rate obtained after iterative convergence, the oxidizer mass flux G_o and the instantaneous regression rate $\dot{r}$ can be calculated by combining the cross section of grain. After integration, parameters of the next moment, such as channel area and flesh thickness, can be obtained. As the combustion efficiency is not known before the test, an initial value is assumed for the calculation. The fuel mass flow rate at each moment is calculated according to the above method and integrated to determine whether the fuel consumption for the entire combustion time is equal to the fuel consumption measured in the test; otherwise, the η_{c*} is adjusted until the given accuracy ε is met:

$$\left| \int_{t_0}^{t_w} \dot{m}_f \mathrm{d}t - m_f \right| \leq \varepsilon \tag{11}$$

$$\dot{r} = \frac{\dot{m}_f}{2\pi\rho L r} \tag{12}$$

where L is the length of the grain. The radius of the grain r can be calculated as:

$$r = r_i + \int_{t_0}^{t} \dot{r} dt \tag{13}$$

After the convergence of iterations, the instantaneous values of the oxidizer mass flux and the regression rate are obtained for the entire test, and the average combustion efficiency of the engine is obtained. Figure 3 shows the flow chart of the entire calculation process.

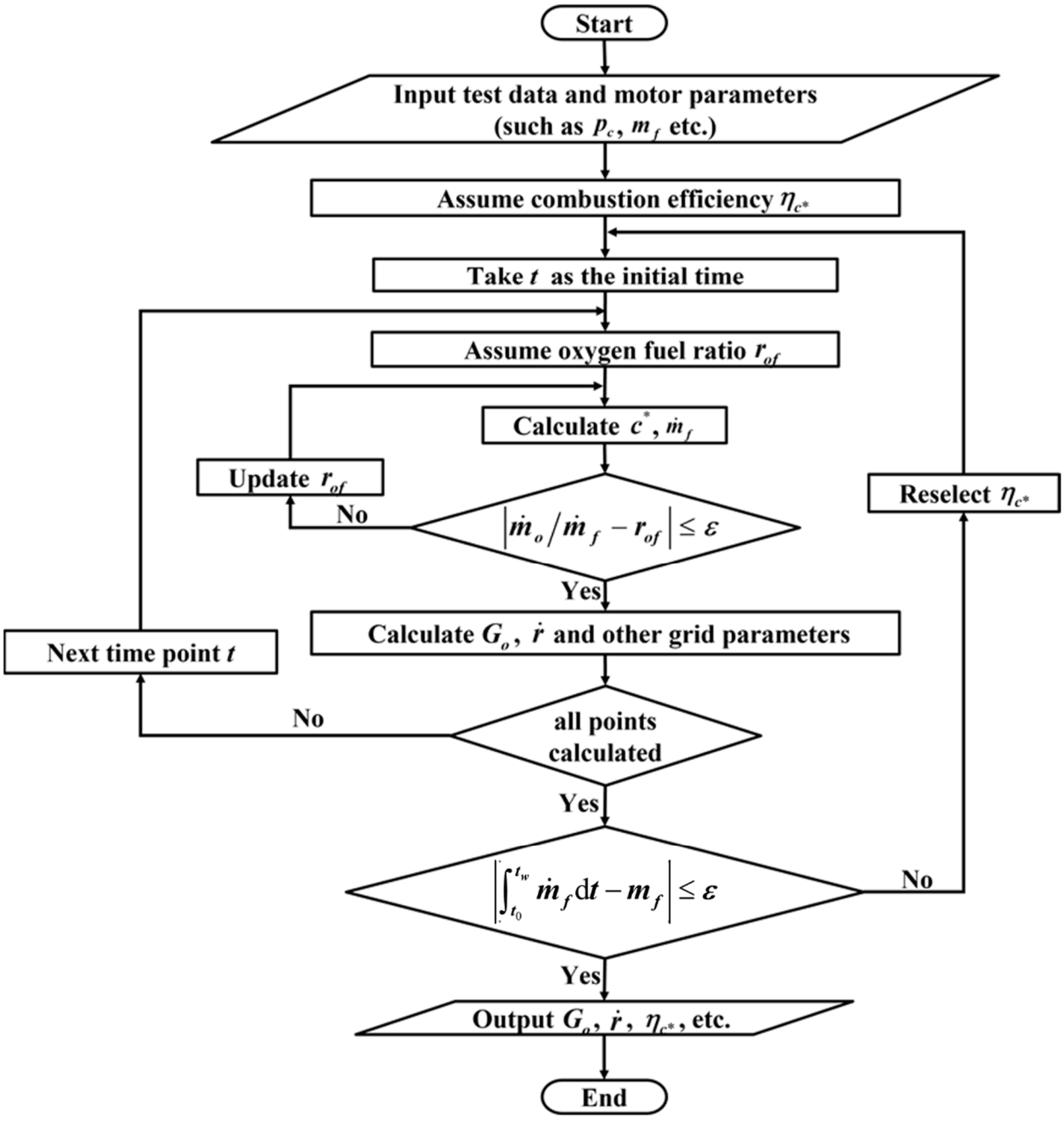

Figure 3. Flow chart for calculating instantaneous regression rate.

4. Results and Discussion

Figure 4 shows the measured combustion chamber pressure and the thrust of the test. The oxidizer valve opening and closing once in a short time is one pulse. In order to achieve a rapid ignition, five pulses are added before ignition to raise the temperature of the catalytic bed, thus promoting the efficiency of the decomposition of hydrogen peroxide. The duration of each pulse is 100 ms, and the gap for each pulse is 600 ms. After five pulses, the oxidizer valve opens at 4.5 s and closes at 9.5 s. The test lasts for five seconds. It is obvious from the combustion chamber pressure curve and thrust curve that an unstable combustion is generated. Furthermore, this oscillation does not occur at the beginning of the engine build-up, but after a period of operation. A possible explanation is that the addition of the high fractional aluminum particles results in an unstable combustion. The unique combustion mechanism of the hybrid rocket motor is diffusion combustion. A vast number of aluminum particles are blown into the flow field as droplets for combustion [24], and the aluminum particles are highly susceptible to coupled oscillations with the airflow. Possible ways to suppress this instability are to reduce the particle size of the aluminum particles and to increase the space of the pre-combustion chamber [25].

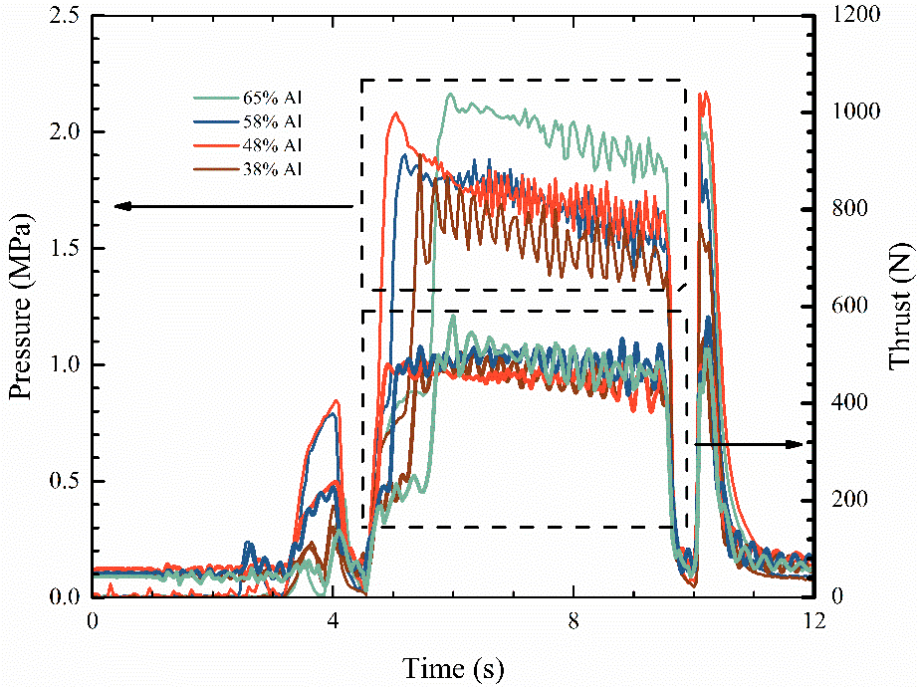

Figure 4. Measured combustion chamber pressure and thrust of test.

Figure 5 shows the instantaneous regression rate versus time and oxidizer mass flux. The instantaneous regression rate in Figure 5a is calculated according to the method described above. As can be seen from Figure 5a, the regression rate shows a general trend of a rapid decline with time. The instantaneous regression rate can be calculated from Equation (7). Therefore, the instantaneous regression rate generally oscillates significantly after the engine has been operating steadily for 1–2 s synchronized with the combustion chamber pressure. As can be seen in Figure 5b, the grain with a 65% mass fraction of aluminum particles decreases from 1.57 mm/s to 1.08 mm/s in the oxidizer mass flux range of 130–160 $kg \cdot s^{-1} \cdot m^{-2}$, which is higher than the grain with 58% and 48% mass fractions of aluminum particles. Furthermore, in the oxidizer mass flux range of 110–130 $kg \cdot s^{-1} \cdot m^{-2}$, the grain with a 65% mass fraction of aluminum particles decreases from 1.08 mm/s to 0.75 mm/s, which is between the grain with 58% and 48% mass fractions of aluminum particles. The regression rate of the grain adding a 38% mass fraction of aluminum particles is between that of the grains with 58% and 48% mass fractions of aluminum particles in the oxidizer mass flux region from 105 $kg \cdot s^{-1} \cdot m^{-2}$ to 120 $kg \cdot s^{-1} \cdot m^{-2}$. Among the four

grains with aluminum particle mass fractions of 38%, 48%, 58%, and 65%, the grain with the mass fraction of 58% decreases the most smoothly with the diminishing oxidizer mass flux. Compared with neat HTPB grains [18], it is clear that the increase in the aluminum mass fraction of the grain enhanced the regression rate. The regression rate of the 90HP and pure HTPB is 0.37 mm/s with an oxidizer mass flux of 93 $kg \cdot s^{-1} \cdot m^{-2}$. The regression rate of the grain with a mass fraction of 38% aluminum particles is 0.56 mm/s, which has increased by 51.35%.

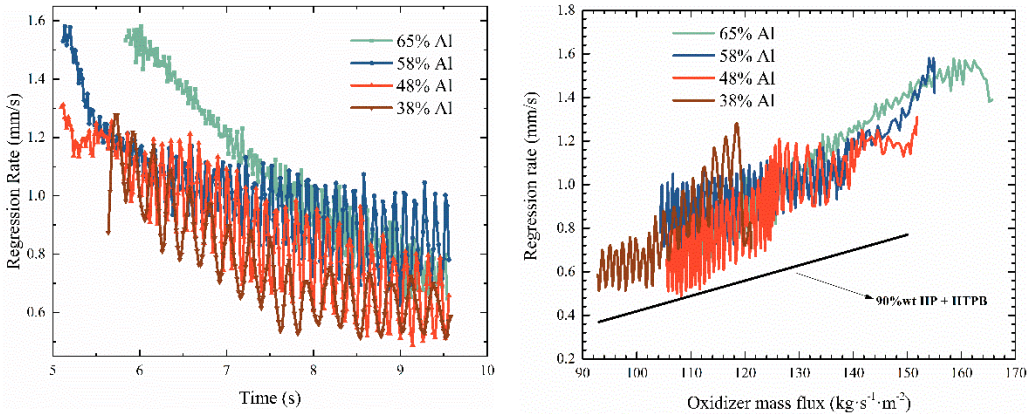

(**a**) (**b**)

Figure 5. Instantaneous regression rate versus time and oxidizer mass flux. (**a**) Instantaneous regression rate versus time. (**b**) Instantaneous regression rate versus oxidizer mass flux.

Table 3 shows the performance results. As can be seen from Table 3, the specific impulses of the hybrid rocket motor with 95% hydrogen peroxide and a combination of 38%, 48%, 58%, and 65% mass fractions of aluminum and HTPB are 185.79 s, 186.82 s, 188.91 s, and 192.46 s, respectively. The average regression rates of the grains containing 38%, 48%, 58%, and 65% mass fractions of aluminum are 0.78 mm/s, 0.96 mm/s, 1.07 mm/s, and 1.12 mm/s, respectively. The addition of aluminum particles leads to an improvement in the specific impulse and regression rate, and the grain with a 58% mass fraction of aluminum particles has the highest combustion efficiency.

Table 3. Performance results.

Fuel	Oxidizer Mass Flow Rate (g/s)	p_c(MPa)	*O/F*	I_{sp} (s)	Average Regression Rate (mm/s)	Combustion Efficiency (%)
38%Al + 62%HTPB	165.2	1.53	3.13	185.79	0.78	87.68
48%Al + 52%HTPB	157.3	1.74	2.71	186.82	0.96	85.35
58%Al + 42%HTPB	155.3	1.70	2.29	188.91	1.07	88.88
65%Al + 35%HTPB	163.3	1.81	1.94	192.46	1.12	85.30

Figure 6 shows the CT scan images of the grains after the test, from which it can be seen that there is a distinct area of end-burning at the front and post-side of all the grains. The end-burning area on the front face is caused by the direct exposure to high-temperature peroxide decomposition products, while the end-burning area on the post-face is attributed to the swirling effect of the post-combustion chamber. The effect of the direct exposure to high-temperature peroxide decomposition products on end-burning at the front face is much more dramatic than the swirling effect of the post-combustion chamber. All four sets of grain CT images in Figure 6 show this trend. Figure 7 shows the axial distribution of the regression rate. The curves in Figure 7 show the effect of removing the front- and rear-end combustion regions. At the front of the grain, the maximum speed of the regression rate occurs. As the axis distance increases, the regression rate decreases rapidly until it reaches

a minimum value, then it increases slowly and gradually decreases. The reasons for this trend are as follows: at the front part of the grain channel, the flame layer is relatively thin and closest to the grain surface, resulting in a high temperature gradient between the flame layer and the grain surface. A higher heat flow density leads to a higher regression rate. However, at the same time, due to the continuous addition of fuel mass flow from the upstream grain, the total mass flow in the grain channel is increasing, which causes an increase in the heat flow. The combined effect of these two factors leads to the above trend in the axial distribution of the regression rate.

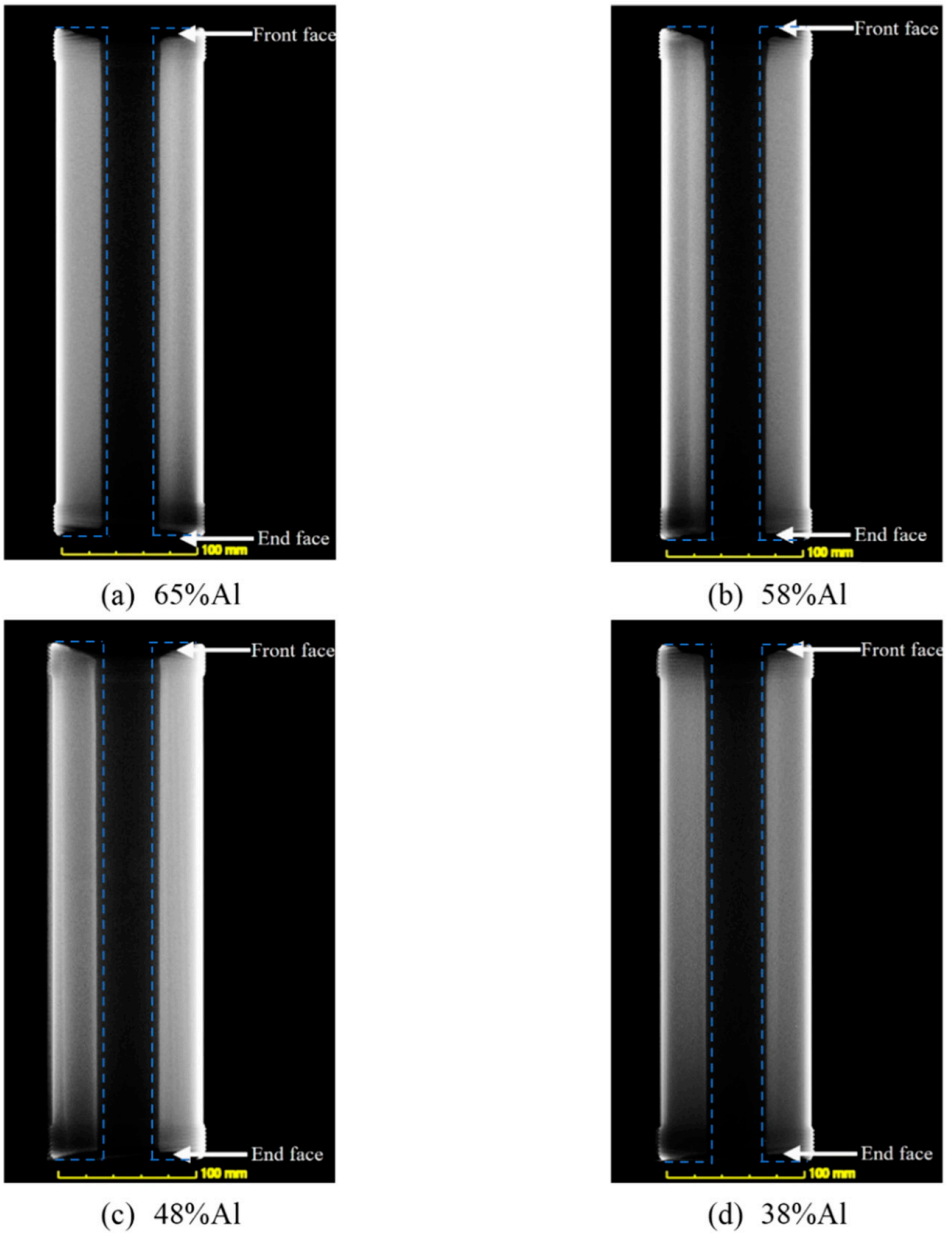

Figure 6. CT scan images of the grains after the test.

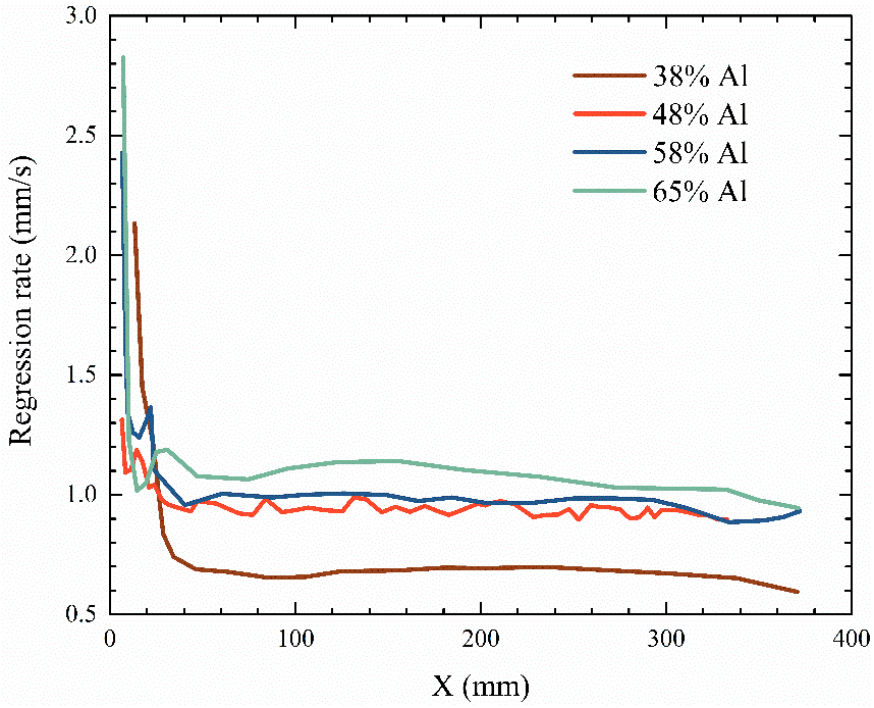

Figure 7. Axial distribution of regression rate.

Figure 8 shows the results of the electron microscopy scan of the grain surface. The spot scans of the electron microscope are repeated three times and the normalized results are shown in the graph. The scanned areas in the graph show that the mass fractions of aluminum on the front surface of the grain after the test are 83.69%, 86.76%, 58.76%, and 51.34% for grains with 65%, 58%, 48%, and 38% mass fractions of aluminum, respectively. It is true that an elemental analysis by electron microscopy cannot detect hydrogen, and the elemental content selected is mainly based on the composition of the main elements blended in the grain before the test; therefore, it will result in a slight overevaluation of the aluminum content on the surface of the grain after the test. The presence of HTPB can be clearly seen on the surface of the grain before the test. After the test, it can be seen that the mass fraction of aluminum on the front surface of the grains is higher than that of the initial mass fraction of the grains, and as the mass fraction of aluminum of the grains increases, the front surface of the post-test grains gradually becomes encapsulated by spherical crystals, making the presence of the HTPB matrix more and more difficult to identify. In addition, the front of the grain is more fully reacted than the post of the grain. The aluminum particles are densely packed on the surface of the front of the grain, while the HTPB matrix has not yet completely retreated below the surface of the back end of the grain, the aluminum and aluminum oxide particles scatter throughout the matrix.

Table 4 shows the parameters of the nozzle after the test. The grains with mass fractions of 38% and 58% aluminum used carbon ceramic nozzles and the grains with mass fractions of 48% and 65% aluminum used tungsten–copper infiltration nozzles. From the data measured before and after the test, the diameter of the carbon ceramic nozzle throat after the test is larger than the throat diameter before the test, and the throat diameter of the tungsten-bronze nozzle after the test is smaller than the throat diameter before the test. The target ignition time for the test is 5 s, but in reality, the steady working time is 4.18, 4.82, 4.55, and 3.87 s due to the ignition delay. The ablation rates are 0.075 mm/s and 0.19 mm/s for carbon ceramic nozzles with grains containing 38% and 58% aluminum mass fractions, respectively, and −0.033 mm/s and −0.099 mm/s for tungsten–copper infiltration nozzles with grains containing 48% and 65% aluminum mass fractions, respectively. The addition of aluminum particles leads to the deposition of particles in the nozzle, while increasing the scouring effect of the particles on the surface of the nozzle throat. For tungsten–copper

infiltration nozzles, the addition of aluminum particles will also enhance the heat flow density of the nozzle throat, which results in the precipitation of copper. The precipitation of copper and the deposition of aluminum oxide particles will lead to the throat diameter becoming smaller, while the scouring of aluminum oxide particles will lead to a larger throat diameter. For the tungsten–copper infiltration nozzle, the overall rate of copper precipitation and deposition of aluminum oxide particles is greater than that of the scouring effect, which ultimately leads to a reduction in the throat diameter. For carbon ceramic nozzles, the scouring effect of the alumina particles is stronger than the deposition effect, thus making the nozzle throat diameter smaller. With the increase in the aluminum particles in the grain, the ablation rate of the carbon ceramic nozzle tends to become larger, and the precipitation rate of tungsten-bronze shows a trend of becoming larger. A more stable throat diameter ensures relatively smooth thrust and motor operating conditions, therefore tungsten-impregnated copper nozzles have a noticeable advantage in engines with a high mass fraction of aluminum particles.

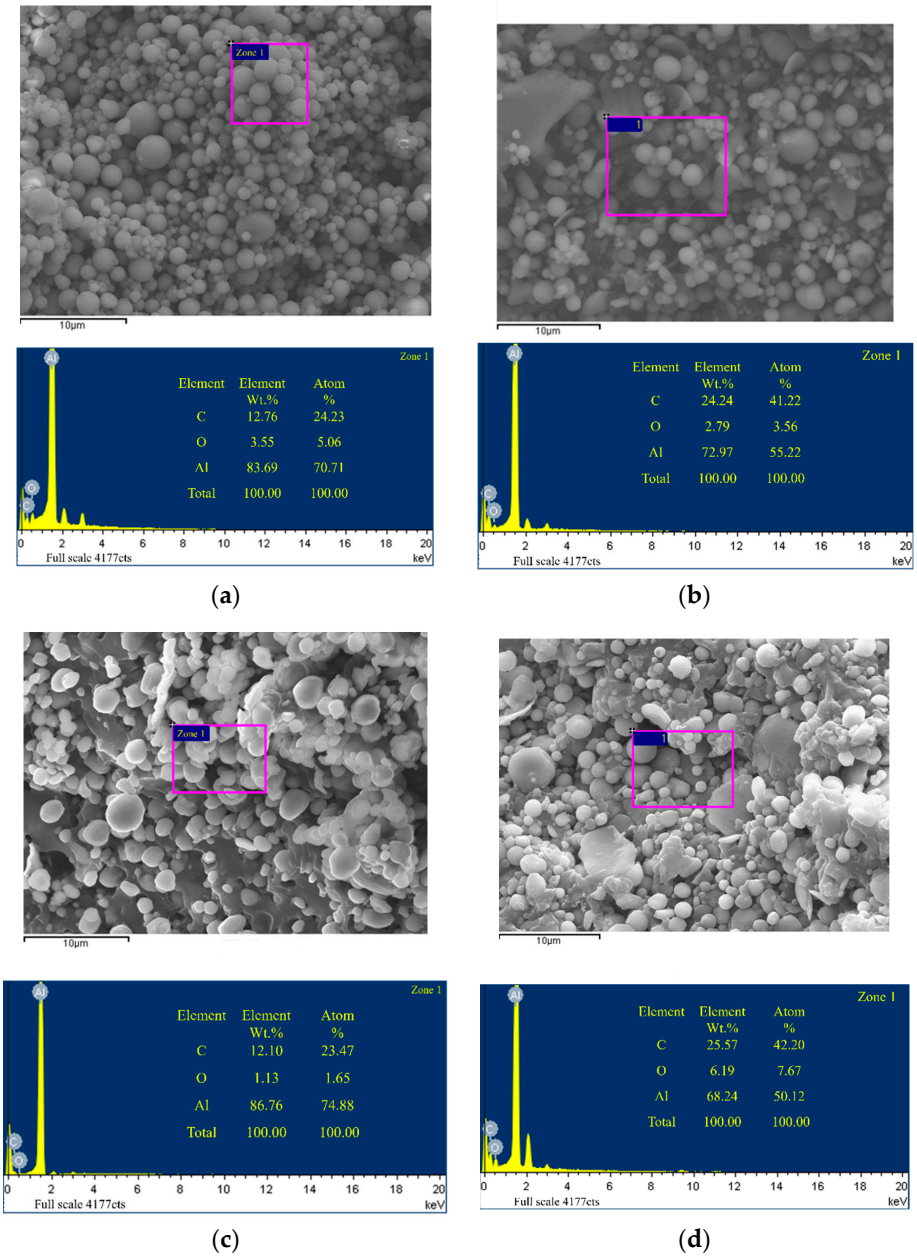

Figure 8. *Cont.*

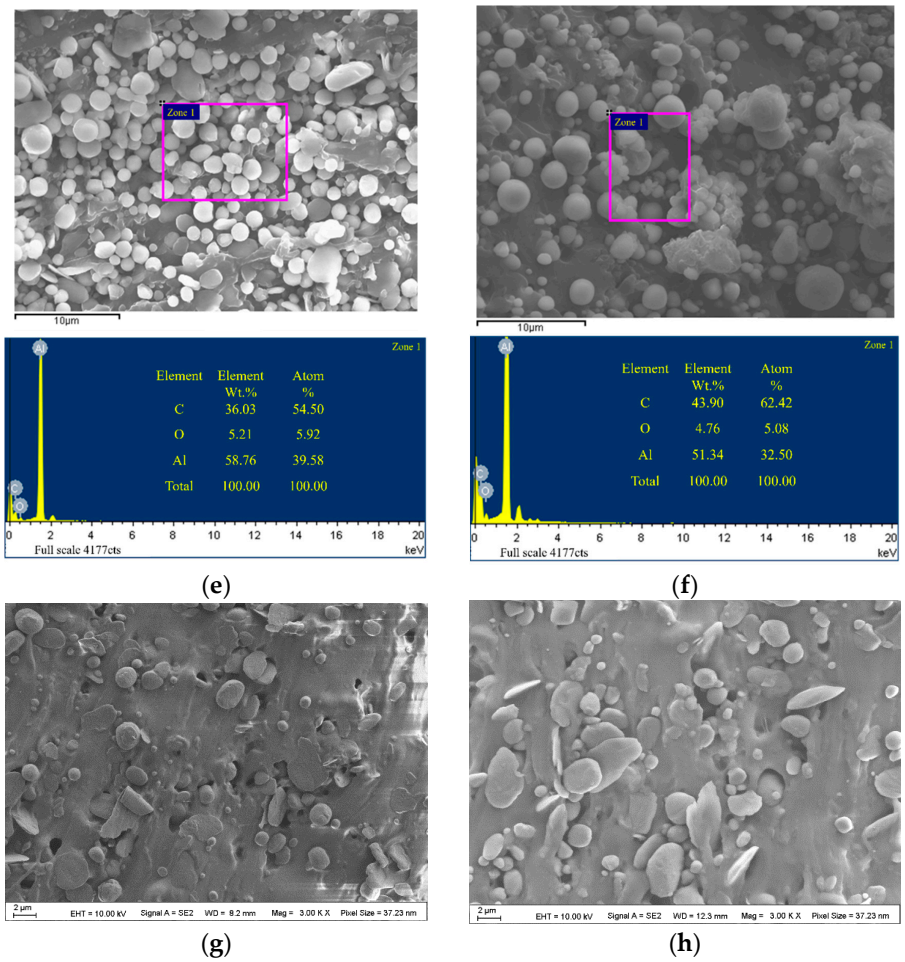

Figure 8. Results of electron microscopy scans of the grain surface. (**a**) 65%Al (front side of grain after test). (**b**) 65%Al (post side of grain after test). (**c**) 58%Al (front side of grain after test). (**d**) 58%Al (post side of grain after test). (**e**) 48%Al (front side of grain after test). (**f**) 38%Al (front side of grain after test). (**g**) 48%Al (front side of grain before test). (**h**) 38%Al (front side of grain before test).

Table 4. Nozzle test results.

Fuel	Nozzle Material	d_1 (mm)	d_2 (mm)	Work Time (s)	Ablation Rate (mm/s)
38%Al + 62%HTPB	Carbon Ceramic	15.293	15.923	4.18	0.075
48%Al + 52%HTPB	Tungsten–copper Infiltration	14.882	14.562	4.82	−0.033
58%Al + 42%HTPB	Carbon Ceramic	14.655	16.152	4.55	0.19
65%Al + 35%HTPB	Tungsten–copper Infiltration	15.002	14.270	3.87	−0.099

5. Conclusions

In this study, the effect of a high mass fraction of aluminum particles on the performance and nozzle ablation of hybrid rocket motors is investigated experimentally. The main conclusions are as follows:

1. The specific impulse of a hybrid rocket motor with 95% hydrogen peroxide and a combination of 38%, 48%, 58%, and 65% mass fractions of aluminum particles and HTPB is 185.79 s, 186.82 s, 188.91 s, and 192.46 s, respectively. The addition of aluminum particles results in an increase in the specific impulse. The addition of aluminum particles decreases the optimal oxygen-to-fuel ratio of the propellant combination, and significantly increases the density-specific impulse in the interval of the oxygen-to-fuel ratio from 1 to 4. The

grain with a 58% mass fraction of aluminum particles has the highest combustion efficiency, which is 88.88%.

2. Due to the lower pyrolysis temperature of HTPB compared with that of the aluminum particles, the aluminum mass fraction on the surface of the grains at the front of the axial position after the test is much higher than that added to the grains before the test. In contrast, the aluminum content on the surface of the axially positioned grains is slightly higher than that added to the grains before the test, indicating that the reaction and heat transfer on the front surface of the grains is more intense compared with the back surface of the grains.

3. The ablation rates of carbon ceramic nozzles with grains containing 38% and 58% aluminum mass fractions are 0.075 mm/s and 0.19 mm/s, respectively, and –0.033 mm/s and –0.099 mm/s for tungsten–copper infiltration nozzles with grains containing 48% and 65% aluminum mass fractions, respectively. The tungsten-impregnated copper nozzle is more resistant to ablation than the carbon ceramic nozzle. After four to five seconds of testing, the tungsten-impregnated copper nozzle shows less variation in throat diameter, which can guide the selection of materials for nozzles for motors containing aluminum.

Author Contributions: Methodology, Y.L.; Formal analysis, H.Z.; Investigation, H.T.; Resources, H.T. and G.C.; Data curation, Z.W. and J.G.; Writing—original draft, Z.W.; Writing—review & editing, H.T. and H.Z.; Project administration, G.C. All authors have read and agreed to the published version of the manuscript.

Funding: This research received no external funding.

Institutional Review Board Statement: Not applicable.

Data Availability Statement: Data is contained within the article.

Conflicts of Interest: The authors declare no conflict of interest.

References

1. Bhadran, A.; Manathara, J.G.; Ramakrishna, P.A. Thrust Control of Lab-Scale Hybrid Rocket Motor with Wax-Aluminum Fuel and Air as Oxidizer. *Aerospace* **2022**, *9*, 474. [CrossRef]
2. Wu, Y.; Yu, X.; Lin, X.; Li, S.; Wei, X.; Zhu, C.; Wu, L. Experimental investigation of fuel composition and mix-enhancer effects on the performance of paraffin-based hybrid rocket motors. *Aerosp. Sci. Technol.* **2018**, *82–83*, 620–627. [CrossRef]
3. Li, M.-C.; Chang, C.-S.; Wei, S.-S.; Wu, J.-S. Experimental Investigation of Throttleable H_2O_2 and Polypropylene Hybrid Rocket Motor. *J. Propuls. Power* **2022**, 1–8. [CrossRef]
4. Hill, C.D.; Nelson, W.; Johansen, C.T. Evaluation of a Paraffin/Nitrous Oxide Hybrid Rocket Motor with a Passive Mixing Device. *J. Propuls. Power* **2022**, *38*, 884–892. [CrossRef]
5. Viscor, T.; Kamps, L.; Yonekura, K.; Isochi, H.; Nagata, H. Large-Scale CAMUI Type Hybrid Rocket Motor Scaling, Modeling, and Test Results. *Aerospace* **2021**, *9*, 1. [CrossRef]
6. Marxman, G.A. Boundary-layer combustion in propulsion. *Symp. Combust.* **1967**, *11*, 269–289. [CrossRef]
7. Marxman, G.A. Combustion in the turbulent boundary layer on a vaporizing surface. *Symp. Combust.* **1965**, *10*, 1337–1349. [CrossRef]
8. Marxman, G.; Muzzy, R.; Wooldridge, C. Fundamentals of hybrid boundary layer combustion. *Prog. Astronaut. Rocket.* **1963**, *15*, 485–522. [CrossRef]
9. Kahraman, M.; Ozkol, I.; Karabeyoglu, M.A. Regression Rate Enhancement of Hybrid Rockets by Introducing Novel Distributed Tube Injector. *J. Propuls. Power* **2022**, *38*, 200–211. [CrossRef]
10. Zhang, Z.; Lin, X.; Wang, Z.; Wu, K.; Luo, J.; Fang, S.; Zhang, C.; Li, F.; Yu, X. Effects of swirl injection on the combustion of a novel composite hybrid rocket fuel grain. *Acta Astronaut.* **2022**, *199*, 174–182. [CrossRef]
11. Li, Z.; Manh, T.D.; Gerdroodbary, M.B.; Nam, N.D.; Moradi, R.; Babazadeh, H. The influence of the wedge shock generator on the vortex structure within the trapezoidal cavity at supersonic flow. *Aerosp. Sci. Technol.* **2020**, *98*, 105695. [CrossRef]
12. Okuda, R.; Komizu, K.; Tsuji, A.; Miwa, T.; Fukada, M.; Yokobori, S.; Soeda, K.; Kamps, L.; Nagata, H. Fuel Regression Characteristics of Axial-Injection End-Burning Hybrid Rocket Using Nitrous Oxide. *J. Propuls. Power* **2022**, *38*, 759–770. [CrossRef]
13. Arves, J.; Jones, H.; Kline, K.; Smith, K.; Slack, T.; Bales, T. Development of a N_2O/HTPB hybrid rocket motor. In Proceedings of the 33rd Joint Propulsion Conference and Exhibit, Seattle, WA, USA, 6–9 July 1997; p. 2803. [CrossRef]
14. Yuasa, S.; Yamamoto, K.; Hachiya, H.; Kitagawa, K.; Oowada, Y. Development of a small sounding hybrid rocket with a swirling-oxidizer-type engine. In Proceedings of the 37th Joint Propulsion Conference and Exhibit, Salt Lake City, UT, USA, 8–11 July 2001; p. 3537. [CrossRef]

15. Zhao, S.; Cai, G.; Tian, H.; Yu, N.; Zeng, P. Experimental Tests of Throttleable H_2O_2/PE Hybrid Rocket Motors. In Proceedings of the 51st AIAA/SAE/ASEE Joint Propulsion Conference, Orlando, FL, USA, 27–29 July 2015; pp. 1–8. [CrossRef]
16. Karabeyoglu, A.; Zilliac, G.; Cantwell, B.J.; DeZilwa, S.; Castellucci, P. Scale-Up Tests of High Regression Rate Paraffin-Based Hybrid Rocket Fuels. *J. Propuls. Power* **2004**, *20*, 1037–1045. [CrossRef]
17. Veale, K.; Adali, S.; Pitot, J.; Brooks, M. A review of the performance and structural considerations of paraffin wax hybrid rocket fuels with additives. *Acta Astronaut.* **2017**, *141*, 196–208. [CrossRef]
18. Farbar, E.; Louwers, J.; Kaya, T. Investigation of Metallized and Nonmetallized Hydroxyl Terminated Polybutadiene/Hydrogen Peroxide Hybrid Rockets. *J. Propuls. Power* **2007**, *23*, 476–486. [CrossRef]
19. Lewin, A.; Dennis, J.; Conley, B.; Suzuki, D. Experimental determination of performance parameters for a polybutadiene/oxygen hybrid rocket. In Proceedings of the 28th Joint Propulsion Conference and Exhibit, Nashville, TN, USA, 6–8 July 1992; p. 3590. [CrossRef]
20. Shark, S.C.; Pourpoint, T.L.; Son, S.; Heister, S.D. Performance of Dicyclopentadiene/H2O2-Based Hybrid Rocket Motors with Metal Hydride Additives. *J. Propuls. Power* **2013**, *29*, 1122–1129. [CrossRef]
21. Risha, G.A.; Evans, B.J.; Boyer, E.; Kuo, K.K. Metals, Energetic additives, and special binders used in solid fuels for hybrid rockets. *Prog. Astronaut. Aeronaut.* **2007**, *218*, 413. [CrossRef]
22. Thomas, J.C.; Petersen, E.L.; Desain, J.D.; Brady, B. Hybrid Rocket Enhancement by Micro- and Nano-Scale Additives in HTPB Fuel Grains. In Proceedings of the 51st AIAA/SAE/ASEE Joint Propulsion Conference, Orlando, FL, USA, 27–29 July 2015; p. 4041. [CrossRef]
23. Tian, H.; Wang, Z.; Guo, Z.; Yu, R.; Cai, G.; Zhang, Y. Effect of metal and metalloid solid-fuel additives on performance and nozzle ablation in a hydroxy-terminated polybutadiene based hybrid rocket motor. *Aerosp. Sci. Technol.* **2022**, *123*, 107493. [CrossRef]
24. Sabnis, J.S. Numerical Simulation of Distributed Combustion in Solid Rocket Motors with Metalized Propellant. *J. Propuls. Power* **2003**, *19*, 48–55. [CrossRef]
25. Karnesky, A.L.; Colucci, S.E. Recent Occurrences of Combustion Instability in Solid Rocket Motors-An Overview. *J. Spacecr. Rocket.* **1975**, *12*, 33–38. [CrossRef]